

# Analysis Note: Projection on $A_1^n$ and $g_1^n$ Measurement at ePIC in the Early Running of EIC

W. Lin<sup>1, 2</sup>

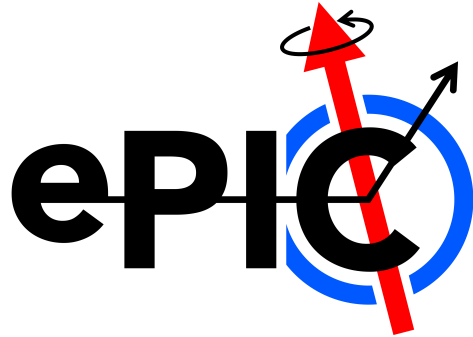
<sup>1</sup>Center for Frontiers in Nuclear Science, Stony Brook University, USA

<sup>2</sup>Department of Physics and Astronomy, Stony Brook University, USA

Summer 2025

## Abstract

The spin structure function  $g_1$  is important for understanding the quark and gluon spin contribution to the overall spin of nucleons. It is also essential for testing the Bjorken sum and provides a unique way of obtaining the strong coupling constant.  $g_1$  can be measured via the longitudinal and transverse double spin asymmetry in a polarized deep inelastic scattering. At the EPIC detector of the future Electron Ion Collider, experiments are planned to obtain high precision  $g_1^p$  and  $g_1^n$  for a large kinematic region from  $ep$  DIS and  $e^3\text{He}$  DIS. In this study, preliminary analysis on  $A_1^n$  and  $g_1^n$  measurement at EPIC early running will be discussed.



## Contents

<b>1</b>	<b>Introduction</b>	<b>1</b>
<b>2</b>	<b>Simulation Overview</b>	<b>5</b>
<b>3</b>	<b>Event Reconstruction</b>	<b>7</b>
3.1	Inclusive Electron . . . . .	8
3.2	Spectator Tagging . . . . .	13
<b>4</b>	<b>Results</b>	<b>16</b>
<b>5</b>	<b>Discussion</b>	<b>20</b>
<b>6</b>	<b>Conclusion</b>	<b>21</b>

# 1 Introduction

The longitudinal spin structure function, denoted as  $g_1$ , is essential for understanding the spin distribution and composition within a nucleon. In the Quark-Parton Model (QPM),  $g_1$  can be expressed as a linear combination of the parton distribution functions (PDFs):

$$g_1(x) = \frac{1}{2} \sum_i e_i^2 \Delta q_i(x) = \frac{1}{2} \sum_i e_i^2 [q_i^\uparrow(x) - q_i^\downarrow(x)] \quad (1)$$

where  $\Delta q_i$  is the PDF of a parton, and  $e_i$  is its charge. The Bjorken scaling,  $x$ , described the fraction of momentum carried by the parton.  $q_i^{\uparrow(\downarrow)}$  is the probability of the parton spin being aligned or anti-aligned with the nucleon spin. Integrating  $g_1$  for the proton and the neutron over the full  $x$  range then gives:

$$\Gamma_1^p = \int_0^1 g_1^p dx = \frac{1}{2} \left( \frac{4}{9} \Delta u + \frac{1}{9} \Delta d + \frac{1}{9} \Delta s + \text{antiquarks} \right) \quad (2)$$

$$\Gamma_1^n = \int_0^1 g_1^n dx = \frac{1}{2} \left( \frac{1}{9} \Delta u + \frac{4}{9} \Delta d + \frac{1}{9} \Delta s + \text{antiquarks} \right) \quad (3)$$

where  $\Delta q_i$  in this case is the first moment of the spin-dependent parton distribution,  $\int_0^1 [q_i^\uparrow(x) - q_i^\downarrow(x)] dx$ . They are related to the weak axial-vector couplings,  $a_0$ ,  $a_3$  and  $a_8$  as followed:

$$a_0 = (\Delta u + \Delta \bar{u}) + (\Delta d + \Delta \bar{d}) + (\Delta s + \Delta \bar{s}) \quad (4)$$

$$a_3 = (\Delta u + \Delta \bar{u}) - (\Delta d + \Delta \bar{d}) \quad (5)$$

$$a_8 = (\Delta u + \Delta \bar{u}) + (\Delta d + \Delta \bar{d}) - 2(\Delta s + \Delta \bar{s}) \quad (6)$$

$a_0$  is then equivalent to the total spin contribution from the quarks for a nucleon. The moment of spin structure function can thus be written as:

$$\Gamma_1^{p(n)} = \frac{1}{12} \left[ +(-)a_3 + \frac{1}{3}a_8 \right] + \frac{1}{9} \Delta \Sigma \quad (7)$$

where  $\Delta \Sigma = a_0$ . If  $\Delta s$  is negligible, i.e.  $a_0 = a_8$ , the integral can be written as  $\Gamma_1^{p(n)} = +(-)\frac{1}{12}(F + D) + \frac{5}{36}(3F - D)$ , where  $F$  and  $D$  are the symmetric and antisymmetric weak  $SU(3)_f$  couplings of the baryon octet. This is called the Ellis-Jaffe sum rule (EJSR) for the proton and the neutron [1, 2], which is proven to be deviated from experimental result leading to the puzzle of the nucleon spin composition.

In Perturbative Quantum Chromodynamics (pQCD),  $g_1$  is described as:

$$g_1(x, t) = \frac{1}{2} \sum_{k=1}^{n_f} \frac{e_k^2}{n_f} \int_x^1 \frac{dy}{y} \left[ C_q^s \left( \frac{x}{y}, \alpha_s(t) \right) \Delta\Sigma + 2n_f C_g \left( \frac{x}{y}, \alpha_s(t) \right) \Delta G(y, t) + C_q^{\text{NS}} \left( \frac{x}{y}, \alpha_s(t) \right) \Delta q_{\text{NS}}(y, t) \right] \quad (8)$$

where  $t = \ln(Q^2/\Lambda^2)$  with  $Q^2$  being the squared four-momentum transfer and  $\Lambda$  being the scale parameter of QCD.  $\alpha_s$  is the strong coupling constant.  $n_f$  is the number of quark flavors.  $C_q$  and  $C_g$  are coefficient functions.  $\Delta q_{\text{NS}}(x, t)$  is the nonsinglet combinations of the polarized quark and antiquark distributions defined to be  $\Delta q_{\text{NS}}(x, t) = \Delta q_i(x, t)[\sum_{i=1}^{n_f}(e_i^2 - \frac{1}{n_f} \sum_{i=1}^{n_f} e_i^2)/(\frac{1}{n_f} \sum_{i=1}^{n_f} e_i^2)]$ . The total spin distribution of the quarks,  $\Delta\Sigma(x, t)$ , and of the gluons,  $\Delta G(x, t)$ , are then related to  $g_1$ . Through the Dokshitzer-Gribov-Lipatov-Altarelli-Parisi (DGLAP) equations which predicts the  $Q^2$  dependence of the quark and gluon distributions, one can deduce information of  $\Delta\Sigma$  and  $\Delta G$  by measuring  $g_1$  [3].

$g_1$  is accessible by measuring the polarized deep inelastic scattering cross section:

$$\frac{d^3\sigma(\beta)}{dQ^2 dx d\phi} = \frac{d^3\sigma_0}{dQ^2 dx d\phi} - \frac{d^3\Delta\sigma(\beta)}{dQ^2 dx d\phi} \quad (9)$$

where the first part of the equation on the right is the unpolarized cross section:

$$\frac{d^2\sigma}{dQ^2 dx} = \frac{4\pi\alpha^2}{Q^4} \frac{1}{x} \left[ xy^2 F_1(x, Q^2) + \left( 1 - y - \frac{Mxy}{2E} F_2(x, Q^2) \right) \right] \quad (10)$$

and the second part is the polarized contribution:

$$\begin{aligned} \frac{d^3\Delta\sigma(\beta)}{dQ^2 dx d\phi} = & \frac{4\alpha^2}{Q^2} y \left\{ \cos\beta \left[ \left( 1 - \frac{y}{2} - \frac{\gamma^2 y^2}{4} \right) g_1(x, Q^2) - \frac{\gamma^2 y}{4} g_2(x, Q^2) \right] \right. \\ & \left. - \cos\phi \sin\beta \frac{\sqrt{Q^2}}{\nu} \left( 1 - y - \frac{\gamma^2 y^2}{4} \right)^{\frac{1}{2}} \left[ \frac{y}{2} g_1(x, Q^2) + g_2(x, Q^2) \right] \right\} \end{aligned} \quad (11)$$

In Eq. 10 and Eq. 11,  $F_1$  and  $F_2$  are the non-polarized structure functions, while  $g_1$  and  $g_2$  are the polarized structure functions.  $\alpha$  is the electromagnetic

coupling constant.  $M$  is the mass of the nucleon, and  $E$  is the energy of the incident electron.  $y$  is the inelasticity which is related to  $x$  and  $Q^2$  by  $Q^2 = sxy$  with  $s$  being the center of mass of the reaction.  $\gamma = 2Mx/\sqrt{Q^2}$  is another kinematic variable.  $\beta$  are the angle between the direction of the incident electron and the and the direction of the nucleon spin.  $\phi$  is the angle between the scattering electron and the nucleon spin [3]. As described, extracting  $g_1$  directly from DIS cross section is possible but difficult because the polarized contribution is small. It is more common to measure  $g_1$  via a double spin asymmetry measurement:

$$\frac{g_1(x, Q^2)}{F_1(X, Q^2)}(1 + \gamma^2) = \gamma A_2(x, Q^2) + A_1(x, Q^2) \quad (12)$$

with

$$A_1(x, Q^2) \equiv \frac{\sigma_{1/2} - \sigma_{3/2}}{\sigma_{1/2} + \sigma_{3/2}} = \frac{A_{\parallel}}{D(1 + \eta\xi)} - \frac{\eta A_{\perp}}{d(1 + \eta\xi)} \quad (13)$$

$$A_2(x, Q^2) \equiv \frac{2\sigma_{LT}}{\sigma_{1/2} + \sigma_{3/2}} = \frac{\xi A_{\parallel}}{D(1 + \eta\xi)} - \frac{A_{\perp}}{d(1 + \eta\xi)} \quad (14)$$

$A_1$  and  $A_2$  are called the virtual photon-nucleon asymmetries.  $\sigma_{1/2}$  and  $\sigma_{3/2}$  refer to the cross section of when the projection of the total spin along the direction of the virtual photon momentum compared to the direction of the nucleon spin is aligned or anti-aligned. Fig. 1 is a demonstration of the two helicity cross sections.  $A_1$  has a much larger contribution to the spin structure function  $g_1$ . This study, similarly to most previous studies, will focus on the projected measurement on  $A_1$  and use an approximation of  $A_1 \approx g_1/F_1$  to project on ePIC's sensitivity to  $g_1$ .

$A_{\parallel}$  and  $A_{\perp}$  are asymmetries that refer to the electron-nucleon spin alignments:

$$A_{\parallel} = \frac{\sigma_{\downarrow\uparrow} - \sigma_{\uparrow\uparrow}}{\sigma_{\downarrow\uparrow} + \sigma_{\uparrow\uparrow}} \quad A_{\perp} = \frac{\sigma_{\downarrow\Rightarrow} - \sigma_{\uparrow\Rightarrow}}{\sigma_{\downarrow\Rightarrow} + \sigma_{\uparrow\Rightarrow}} \quad (15)$$

In these equations, the arrows indicate the alignment of the electron and nucleon spins. The rest of the variables in Eq. 13 are kinematic variables:

$$D = \frac{y(2 - y)(2 + \gamma^2 y)}{2(1 + \gamma^2)y^2 + (4(1 - y) - \gamma^2 y^2)(1 + R)} \quad (16)$$

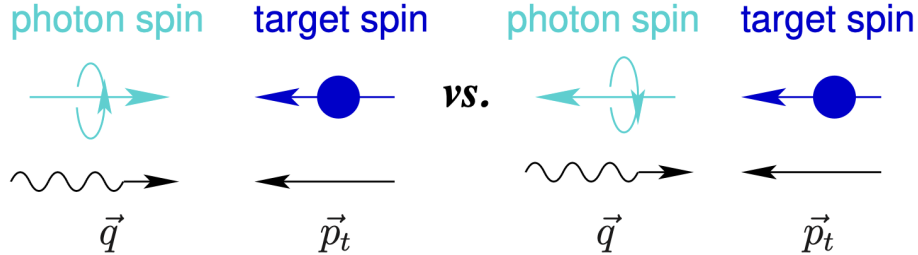


Figure 1: Demonstration of the photon-nucleon spin alignment for  $\sigma_{1/2}$  versus  $\sigma_{3/2}$ . Black arrows are the momentum vector directions. The dark blue arrow is the direction of the nucleon spin. Light blue circular arrow indicate the spin of the virtual photon, and light blue arrow is the projection along the direction of the virtual photon momentum [4].

$$d = \frac{D\sqrt{4(1-y) - \gamma^2 y^2}}{2-y} \quad \eta = \frac{4(1-y) - \gamma^2 y^2}{(2-y)(2+\gamma^2 y)} \quad \xi = \frac{\gamma(2-y)}{2+\gamma^2 y} \quad (17)$$

$D$  is called the depolarization factor of the virtual photon, and  $R$  used in its calculation is the ratio of the longitudinal to transverse virtual photon absorption cross sections:

$$R \equiv \frac{\sigma_L}{\sigma_T} = \frac{(1+\gamma^2)F_2 - 2xF_1}{2xF_1} \quad (18)$$

The importance of measuring  $g_1$  is demonstrated in earlier part in this section, and through double spin asymmetry,  $g_1$  can be calculated as shown in Eq. 12, 13 and 15. In this analysis note, the study focuses on the projected measurement for the neutron spin structure. In the existing experiments,  $g_1$  for protons are and neutrons are measured but were at relatively high  $x$ . In order to understand the nucleon spin structure and the composition of its spin, high precision low  $x$  measurements is needed to reveal the low  $x$  behaviour of  $g_1$  and suppressed the uncertainties in  $\Delta\Sigma$  and  $\Delta G$ . ePIC at EIC will be able to provide these low  $x$  data with wide  $Q^2$  coverage which will be shown in the following sections. (Need to add some description of early science program and double tagging..)

Year	Species	Energy (GeV)	Luminosity ( $fb^{-1}$ )	$e^-$ polarization	$p/A$ polarization
1	eRu/Ag	10x115	0.9	No (commissioning)	N/A
2	eD	10x130	11.4	LONG	NO
	ep		4.95-5.33		TRANS
3	ep	10x130	4.95-5.33	LONG	TRANS and/or LONG
4	eAu	10x100	0.84	LONG	N/A
	ep	10x250	6.19-9.18		TRANS and/or LONG
5	eAu	10x100	0.84	LONG	N/A
	eHe3	10x166	8.65		TRANS and/or LONG

Table 1: EIC early science program

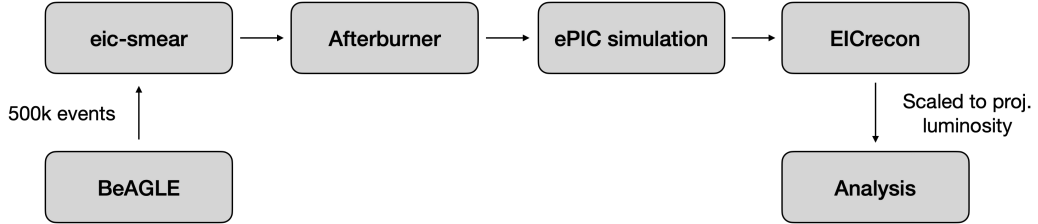


Figure 2: Simulation and analysis chain.

## 2 Simulation Overview

To project the  $A_1^n$  and  $g_1^n$  measurement in year 5 of EIC running,  $e^3\text{He}$  DIS events with  $10 \times 166 \text{ GeV/nucleon}$  are generated and ran through the full EPIC simulation analysis chain as shown in Fig. 2. The events are first generated using an  $eA$  non-polarized scattering event generator, BeAGLE [5]. Comparing to other generators used in similar studies, BeAGLE has more handling on nuclear effects including nuclear breakup, Fermi motion, short-range correlations, partonic gluon radiation, hadronic cascade and more. It employs PYTHIA6 [6] to handle the elementary particle interaction, and Currently, does not simulate radiative effect. In this study, estimated the statistical uncertainty of the double spin asymmetry is estimated by:

$$\delta A_{\parallel,\perp} = \frac{1}{\sqrt{N P_e P_N}} \quad (19)$$

where  $N$  is the number of events in a kinematic bin of the non-polarized DIS simulation generated using BeAGLE.  $P_e$  and  $P_N$  are polarizations of the electron and helium-3 beams, which are assumed to be 70% as indicated by the EIC yellow report [7]. The uncertainties are then propagate to  $A_1^n$  following the relation between  $A_1^n$  and the double spin asymmetries stated in Eq. 13.

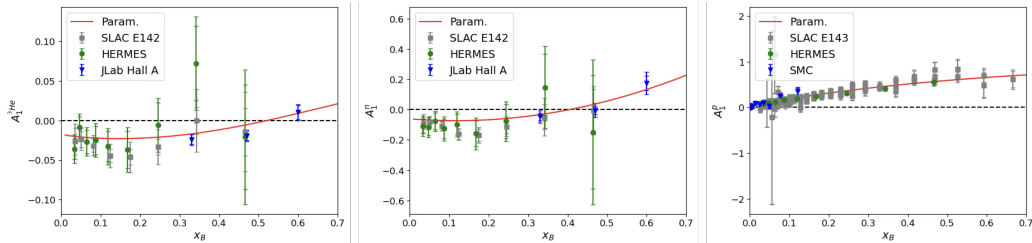


Figure 3: Parameterization used for central value of  $A_1$  compared to existing data [8–13]. The red parameterization data is calculated at  $Q^2 = 2.88$  GeV $^2$ . Data are at various  $Q^2$  values with majority of events near  $Q^2 = 2.88$  GeV $^2$ .

For an outlook of what the asymmetry result will look like, parameterization from world data fit is used to plot the central value of  $A_1^n$  [8]. To compare the  $A_1^n$  obtained using the double spectator tagging method with the traditional method of extraction from  $A_1^{^3\text{He}}$ ,  $A_1^{^3\text{He}}$  is calculated from  $A_1^p$  and  $A_1^n$  using a simple  ${}^3\text{He}$  model:

$$A_1^{^3\text{He}} = P_n \frac{F_2^n}{F_2^{^3\text{He}}} A_1^n + 2P_p \frac{F_2^p}{F_2^{^3\text{He}}} A_1^p \quad (20)$$

where  $F_2^p$ ,  $F_2^n$  and  $F_2^{^3\text{He}}$  are non-polarized structure functions of a proton, a neutron, and a  ${}^3\text{He}$  respectively.  $P_n = 0.86 \pm 0.02$  and  $P_p = -0.028 \pm 0.004$  are the effective nucleon polarization in  ${}^3\text{He}$  calculated from world data [14]. Figure 3 shows the asymmetry for  $A_1^p$ ,  $A_1^n$  and  $A_1^{^3\text{He}}$  using the parameterization compared to existing data. For projection of  $g_1^n$ , an approximation of  $g_1^n \approx A_1^n \cdot F_1$  is used to plot the central values of  $g_1^n$ . For this study, all the structure functions are taken from the JAM22 world fit [15] and evaluated at the  $x$  and  $Q^2$  bins using LHAPDF [16].

To get statistics at higher  $x$  and  $Q^2$  region while reducing computational cost and file size, the events are generated separately for three kinematic regions as shown in Fig. 4. Later the samples are scaled to luminosity

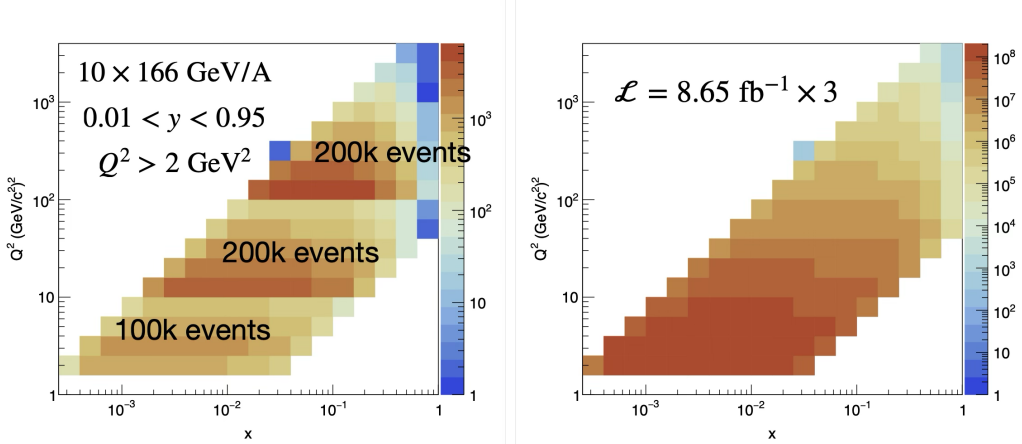


Figure 4: Generated  $e^3\text{He}$  scattering events from BeAGLE. **Left:** Raw data from generator before scaling to desired luminosity. Number of events generated in each kinematic region are indicated by text in the figure. **Right:** Data after scaling to beam luminosity of  $\mathcal{L} = 8.65 \text{ fb}^{-1} \times 3$  nucleons.

of  $\mathcal{L} = 8.65 \text{ fb}^{-1}/\text{nucleon}$ , which is currently planned for EIC year-5 running. In the next step of the simulation, the generated files are converted to HEPMC3 [17] using EIC-smear, and fed to Afterburner for crossing angle and beam smearing effects. Next, EPIC simulation [18] is used for simulating detector output, and the outputs are analysed by EICrecon for event reconstruction<sup>1</sup>. Taking the event information from EICrecon, the scattering kinematic reconstruction, tagging and physics analysis are done in separate code outside of EICrecon, which can be found on GitHub.

### 3 Event Reconstruction

Kinematic cuts are applied to data that require  $0.01 < y < 0.95$ ,  $Q^2 \geq 2$  and  $W^2 > 4$  to select the region with realistic detector acceptance and DIS kinematics. To identify the  $en$  scattering events, double spectator proton tagging is applied. Currently, the analysis uses a simple tagging method as discussed in Sec. 3.2, as the tracking for the Far Forward detector for  ${}^3\text{He}$  is not ready at the moment. In the next couple of subsections, the procedures

---

<sup>1</sup>In this study, EPIC simulation and EICrecon are ran by the simulation campaign: EPIC 25.03.1.

of reconstructing event kinematics from the scattered electrons, the spectator tagging, and the qualities of the event reconstruction are discussed.

### 3.1 Inclusive Electron

Algorithm	$Q^2$	Inelasticity $y$	Bjorken $x$
Electron (E)	$2E_0 E_e (1 + \cos \theta_e)$	$1 - \frac{E_e(1-\cos \theta_e)}{2E_0}$	$\frac{Q^2}{4E_0 E_e y}$
Jacquet-Blondel (JB)	$\frac{p_{t,h}^2}{1-y}$	$\frac{\delta_h}{2E_0}$	
Double-Angle (DA)	$\frac{4E_0^2}{\tan(\frac{\theta_e}{2})(\tan(\frac{\theta_e}{2})+\delta_h/p_{t,h})}$	$\frac{\delta_h/p_{t,h}}{\tan(\frac{\theta_e}{2})+\delta_h/p_{t,h}}$	
Sigma ( $\Sigma$ )	$\frac{E_e^2 \sin^2 \theta_e}{1-y}$	$\frac{\delta_h}{\delta_h+E_e(1-\cos \theta_e)}$	
E-Sigma ( $e\Sigma$ )	$Q_E^2$	$\frac{Q_E^2}{4E_0 E_e x_\Sigma}$	$x_\Sigma$

Table 2: Inclusive electron reconstruction algorithms.  $E_0$  is the initial energy of the electron, while  $E_e$  and  $\theta_e$  are energy and angle of the scattering electron.  $p_{t,h}^2 = (\sum_h p_{x,h})^2 + (\sum_h p_{y,h})^2$  is summing the  $x$  and  $y$  components of the momentum vector for all the hadronic final states.  $\delta_h = \sum_h E_h - p_{z,h}$  is the sum of difference between hadronic final state energies and their  $z$  components of the momentum vector.

As the particle identification analysis is under development, in this analysis, MC information is used for identifying the scattered electron by assuming the first outgoing electron in the simulated event is the scattered electron. MC information is also used for pairing tracks and calorimeter information. To reconstruct the kinematics, five different algorithms are tested: Electron (E), Jacquet-Blondel (JB), Double-Angle (DA), Sigma ( $\Sigma$ ) and E-Sigma ( $e\Sigma$ ) methods. These methods obtain the scattering angles ( $\theta_e$ ) from the trackers, and scattered electron energies ( $E_e$ ) from the tracker or calorimeter to reconstruct  $Q^2$  and  $y$ . And From them, the Bjorken  $x$  is reconstructed. In the fully inclusive E-method, only the information of the scattering electron is used for the reconstruction, while the JB-method uses information of the hadronic

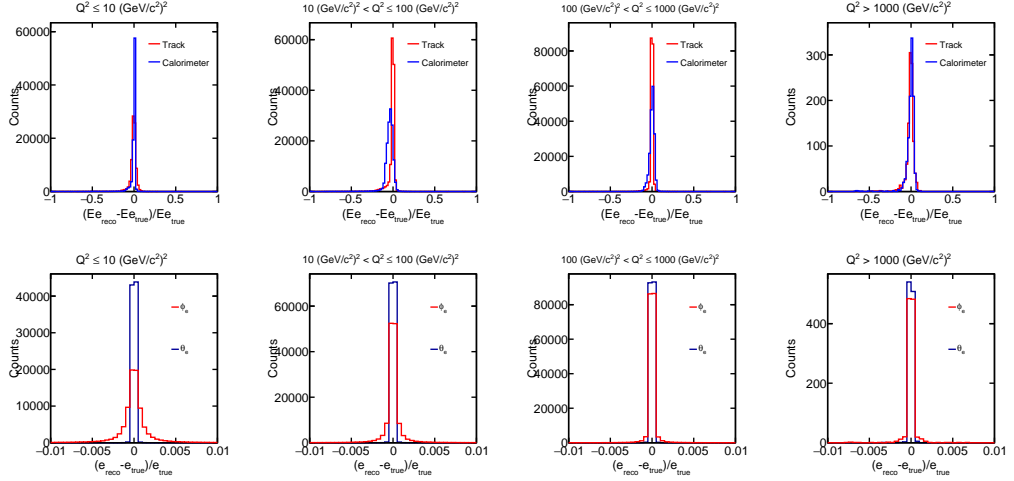


Figure 5: Scattered electron energy and angle resolution. **Top four:** Energy obtained from tracks versus from calorimeter cluster at four  $Q^2$  range. **Bottom four:** Reconstructed scattering angles,  $\theta$  and  $\phi$ , from tracking at four  $Q^2$  range.

final state particles (HFS) and completely ignores the inclusive electron. The DA-method takes the electron scattering angles but ignores its energy, and the  $\Sigma$ -method avoids making assumptions of the incoming electron energy,  $E_0$ , which gives it more resistance to QED radiation. Finally, the  $e\Sigma$ -method combines the  $Q^2$  from the  $E$ -method and  $x$  from the  $\Sigma$ -method to construct the inelastic  $y$ . Table 2 lists the calculation of the kinematic variables  $Q^2$ ,  $x$  and  $y$  for these algorithms.

The scattering electron energy can be obtained from tracking or calorimeter as mentioned. Figure 5 compares the energy resolution between tracking and calorimeter result at different  $Q^2$ . At lower  $Q^2$  where the scattering angle of the electron is small, the end cap detectors are used for tracking which is less precise compared to the tracking detectors in the barrel. At this region, the calorimeter reports energy far more accurate than the tracking. As shown at the bottom four plots in Fig. 5, resolution of the angle of the track,  $\phi$ , increases as  $Q^2$  increases, hence, the resolution of tracking increases. At higher  $Q^2$  gives result comparable to or surpassing the calorimeter. The comparison of scattering electron reconstruction between tracking and calorimeter clusters can also be seen in Fig. 6 where the energy resolutions versus the scattering angle are plotted. In addition to the change of the resolution as scattering angles changes, inefficiency in reconstructing the energy at about  $\theta$

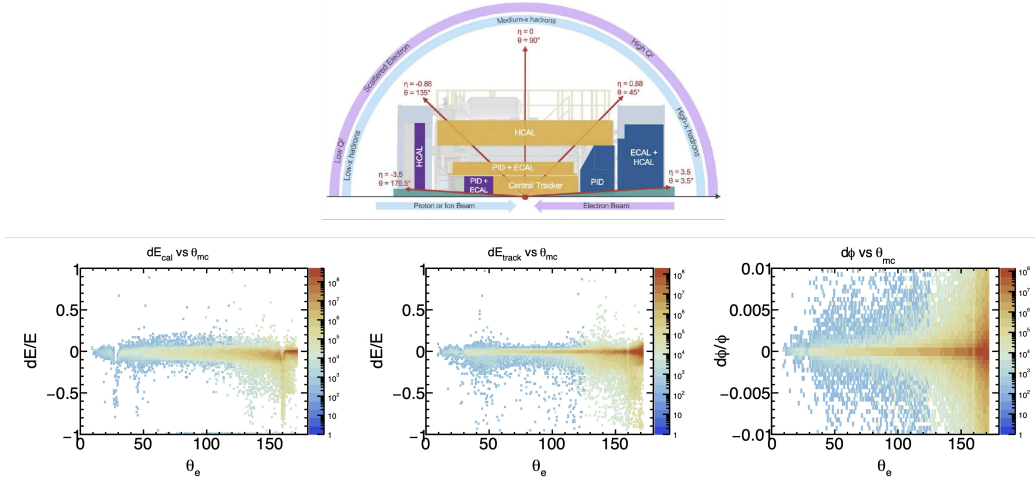


Figure 6: Quality of the scattering electron energy reconstruction as a function of true scattering angle,  $\theta_e$ . **Top:** schematic drawing of different ePIC central detector system angular coverage. **Bottom left:** energy resolution from cluster. **Bottom middle:** energy resolution from tracking. **Bottom right:** resolution of the reconstructed track angle,  $\phi$ .

of  $35^\circ$  and  $135^\circ$  is observed. The inefficiency occurs at the where the tracking information switched from extracting from barrel detectors to the end caps. This acceptance effect will be reduced or corrected in the future development of simulation and analysis. To optimize the reconstruction of the scattering electron, the scattered electron energy used in the calculation is chosen from the calorimeter or tracking based on Fig. 6. The energy and momentum reconstruction qualities for the HFS particles are also checked as indicated in Fig. 7, where the resolution of the energy and momentum components with respect to the true MC information are plotted. The figure shows that the resolutions for HFS reconstruction are generally good. The forward region has decreasing resolution and small amount of failed reconstruction.

Figure 8 shows the reconstructed  $Q^2$ ,  $x$  and  $y$  values compared to the true MC values. The off-diagonal events are caused by the occasional poor track and energy reconstruction from the detectors. If a cut is applied to select out the well reconstructed events, the off-diagonal events are removed as shown in Fig. 9. The advantage of using different reconstruction algorithms is that while the electron method is relatively simple as it only needs the scattering electrons, it is also more vulnerable by Bremsstrahlung radiation because the

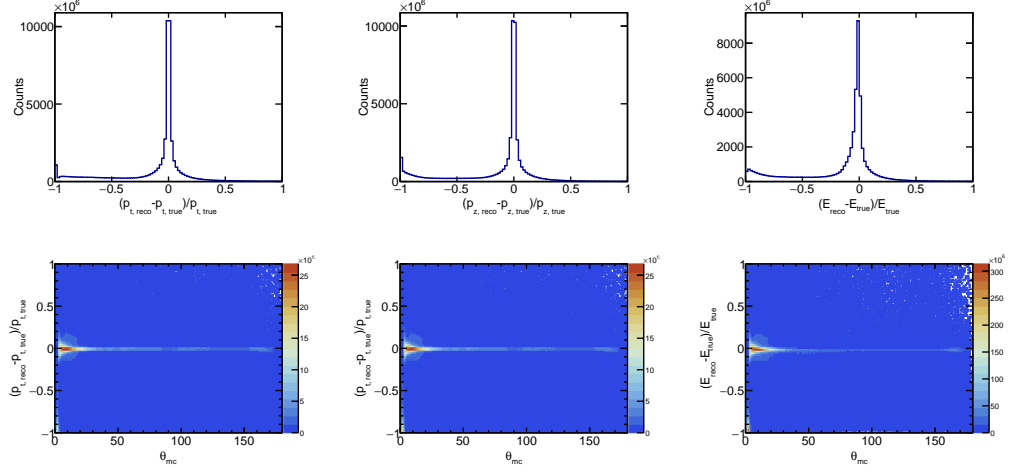


Figure 7: Quality of the hadronic final states reconstruction. **Top three:** resolution of  $p_t$ ,  $p_z$  and energy for each HFS particles. **Bottom three:** resolution of  $p_t$ ,  $p_z$  and energy for each HFS particles versus their true scattering angles.

beam energy is assumed. Other reconstruction algorithms replying less on the incoming electron are more resistive to QED radiative, but there are more particles involved and reconstruction resolution of HFS are generally worse than the inclusive electron. Hence, to minimize the uncertainty of the final physics result, multiple reconstruction algorithms are compared to select the best one to use at a particular kinematic region. In general, the  $E$ -method are better at the high- $y$  region, while other method uses HFS information surpass at lower  $y$ . This is because the HFS methods are constructed in such a way that it is more dependent on high  $p_t$  particles in case the high  $p_z$  particles traveling in the beam direction are missed. The low  $y$  region correspond to when the struck quark has lower  $p_t$  and higher  $p_z$ , hence, methodes uses HFS information perform well at this region. Figure 10 shows the method that has the highest fraction of events reconstructed to the correct  $x$  and  $Q^2$  bins. Analysis determines which algorithm to use based on this histogram and the real MC kinematic<sup>2</sup> in order to maximized the number of correctly reconstructed events in each bin.

After selecting to use energies information from tracking or calorimeter,

---

<sup>2</sup>in real analysis with experimental data, a more mature way of determining the algorithm without MC information will be implemented.

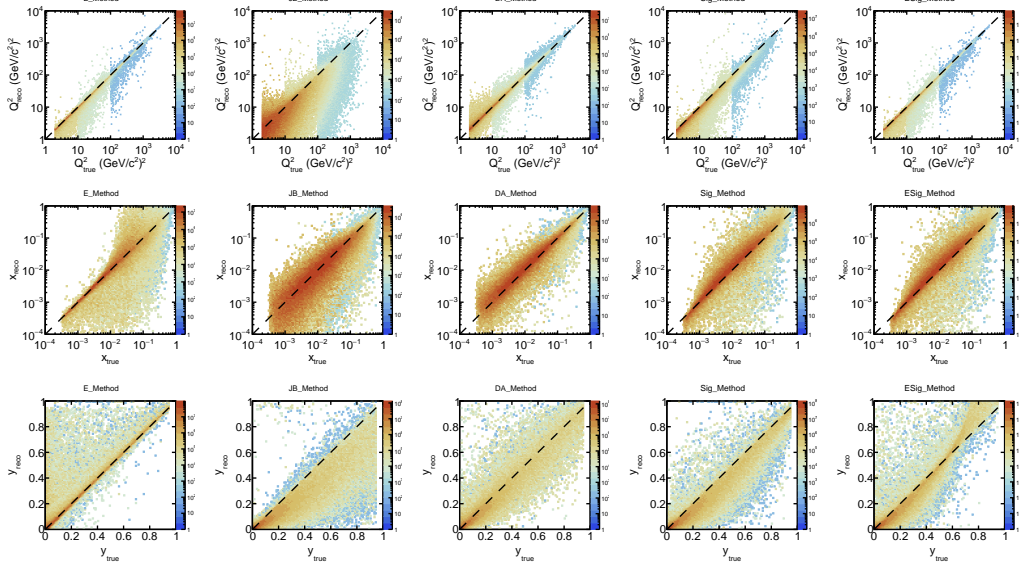


Figure 8: Reconstructed  $Q^2$ ,  $x$  and  $y$  versus their real values for the five reconstruction algorithms.

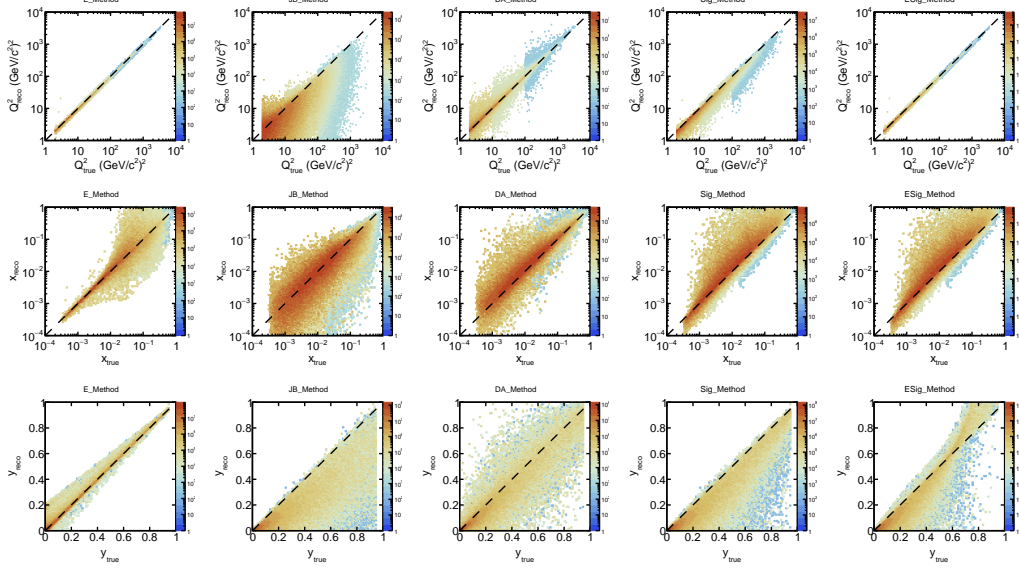


Figure 9: Reconstructed kinematics versus their real values after applying cuts to remove events with significantly insufficient energy or tracking reconstructions.

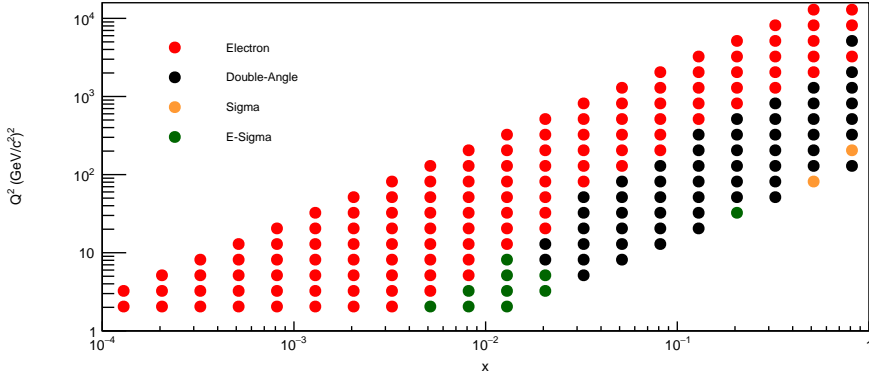


Figure 10: Highest efficiency algorithm for each kinematic bin. Efficiency is determined by the number of events reconstructed in the correct bin using each reconstruction algorithm over the true number of events in the bin calculated using MC information.

and picking the reconstruction algorithm, efficiency and purity of the overall kinematic reconstruction are calculated. (Ugh oh need to add this ..)

### 3.2 Spectator Tagging

To identify the events with electron scattering off a mostly free neutron inside the  ${}^3\text{He}$ , the Roman Pots (RP) and Off-Momentum Detectors (OMD) in the far-forward region are used to tag the low  $p_t$  protons as shown in Fig. 13. These detectors are made out of AC-coupled Low-Gain Avalanche Diode (AC-LGAD) with Application-Specific Integrated Circuit (ASIC) readouts. There are four planes of RP, with two planes located at roughly 32.5 m and two other planes at 34.2 m away the interaction point in the hadron beam direction. Similarly, the forward two-plane station of the OMD is located at about 22.5 m and the backward two planes are at 24.5 m [7]. Because of the beam rigidity change after the  $A_1 {}^3\text{He}$  breakup, the spectator protons will travel down the beam line in the more  $-x$  direction, hitting the left edge of the RP and right edge of the OMD (in  $+z$  direction) as shown in Fig 12.

In the current simple tagging method, for each event, the number of hits on each detector plane is checked. The number of proton tracks is defined to be the minimum number of hits of the four planes of the RP or OMD detectors. If there are at least two proton tracks, the event is tagged as

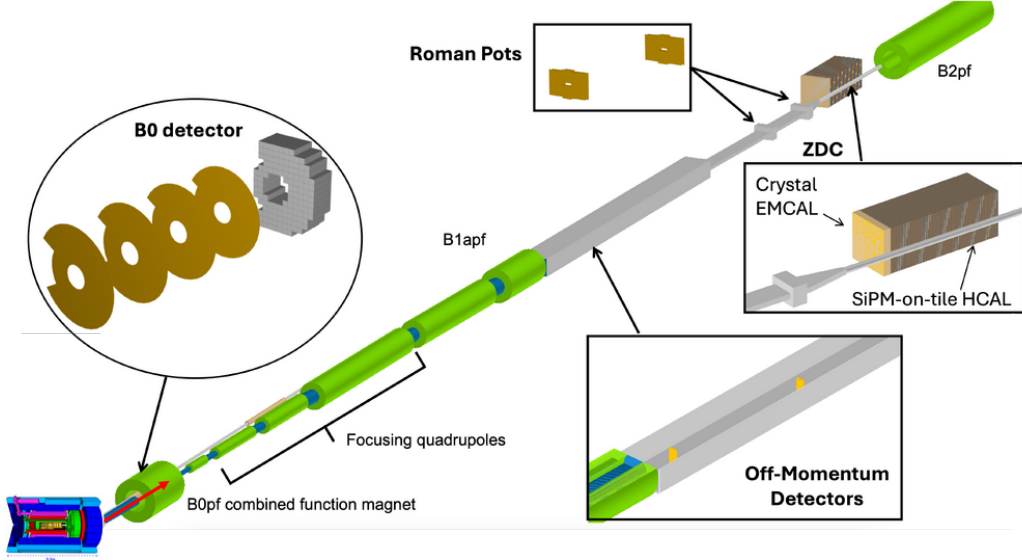


Figure 11: Schematic of the ePIC Far-Forward detector subsystem from ePIC simulation. Roman Pots and Off-Momentum detectors are used for the double spectator proton tagging.

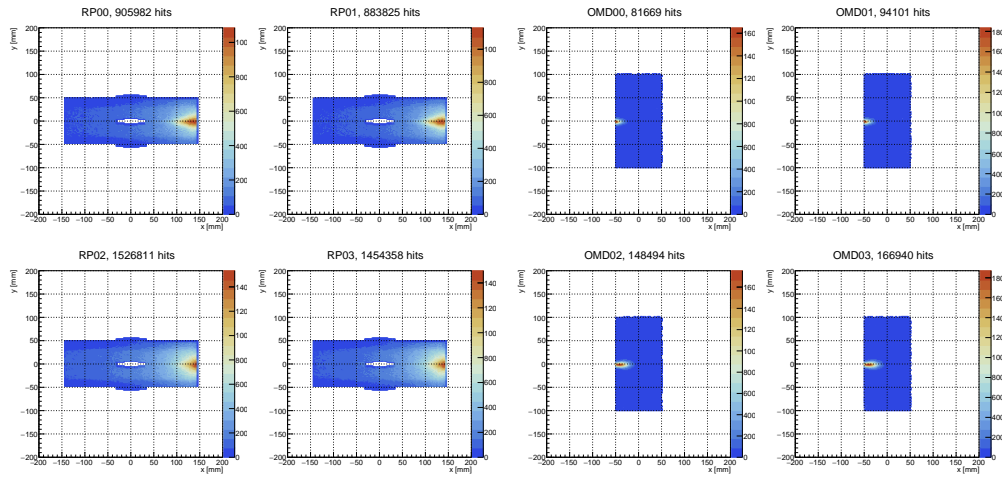


Figure 12: Hits on Roman Pot and Off-Momentum Detector planes for  $10 \text{ GeV}^2 < Q^2 < 100 \text{ GeV}^2$  in the detector local coordinates. Smaller detector number in the title is located closer to the central detectors, and larger detector number is farther away.

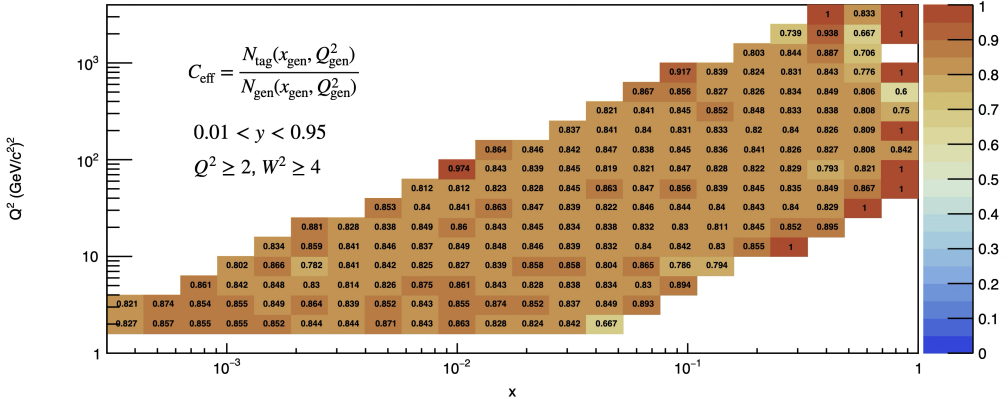


Figure 13: Tagging efficiency,  $C_{\text{eff}}$ , for the simple plane-hit tagging method.  $N_{\text{gen}}$  is the number of generated  $en$  scattering events in each bin.  $N_{\text{tag}}$  is the number of tagged events where the kinematics is reconstructed using generator information.

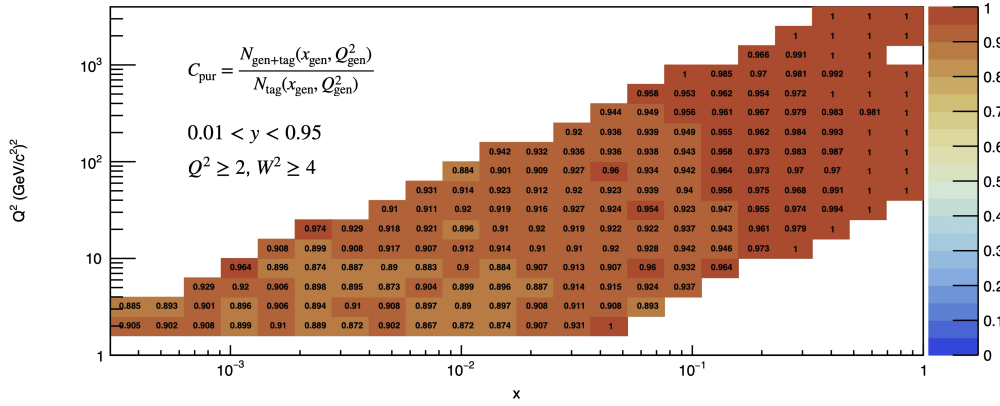


Figure 14: Tagging purity,  $C_{\text{pur}}$ , for the simple plane-hit tagging method.  $N_{\text{tag}}$  is the number of tagged events in each bin.  $N_{\text{tag+gen}}$  is the number of correctly tagged events. The  $x_{\text{gen}}$  and  $Q^2_{\text{gen}}$  of each bin are reconstructed using generator information.

*en* scattering. Figure 13 shows the tagging efficiency of each  $x$  and  $Q^2$  bin by comparing the number of generated events and the number of tagged events. The efficiency is fairly uniform across the kinematic region and more than 80% of the neutron events are tagged. Figure 14 shows the fraction of events that are tagged correctly out of the total tagged events for each kinematic bin is greater than 90%, with lower  $x$  and  $Q^2$  being slightly less accurate and higher  $x$  and  $Q^2$  being most efficient in identify *en* scattering events. The tagging efficiency and purity will be improved by using proper tracking algorithm making use of detector hit positions and magnetic field. More details about inefficiency of current simple tagging method and future tagging algorithm will be discussed in Sec. 5.

## 4 Results

After reconstructing the DIS kinematic and identifying the *en* DIS events from double spectator tagging, the selected events are scaled to a beam luminosity of  $\mathcal{L} = 8.65 \text{ fb}^{-1}$  per nucleon as mentioned in Sec. 2. The scaled statistics are used to project the statistical uncertainty on  $A_1^n$  using Eq. 20. Figure. 15 shows improvement in  $A_1^n$  uncertainty by doing double tagging. In this figure, the statistical uncertainty and the model uncertainties from the structure functions are included. Comparing the two algorithm for extracting the  $A_1^n$ , the double tagging method reduces the overall uncertainty by 50% to 70%.

A projection of the  $A_1^n$  result in year five of EIC early science with estimated statistical uncertainty from  $e^3\text{He}$  polarized measurement using the double spectator tagging method is given in Fig. 16. As shown, ePIC will measure  $A_1^n$  with good statistical uncertainty at low  $x$  and  $Q^2$  region uncovering phase space that currently has no polarized neutron spin asymmetry data, while overlaps with kinematic region with previous measurement to check data consistency. After the first five year running, EIC will have more data on the neutron spin measurement with wider kinematic coverage.

To project the statistical uncertainty that ePIC will get on  $g_1^n$  at the first five year running of EIC, approximation of  $g_1^n = A_1^n \cdot F_1^n$  is used. Figure 17 shows the projected uncertainty on  $g_1^n$  at various  $Q^2$  as a function of  $x$  where the  $F_1^n$  structure function is taken from the JAM22 global fit [15].

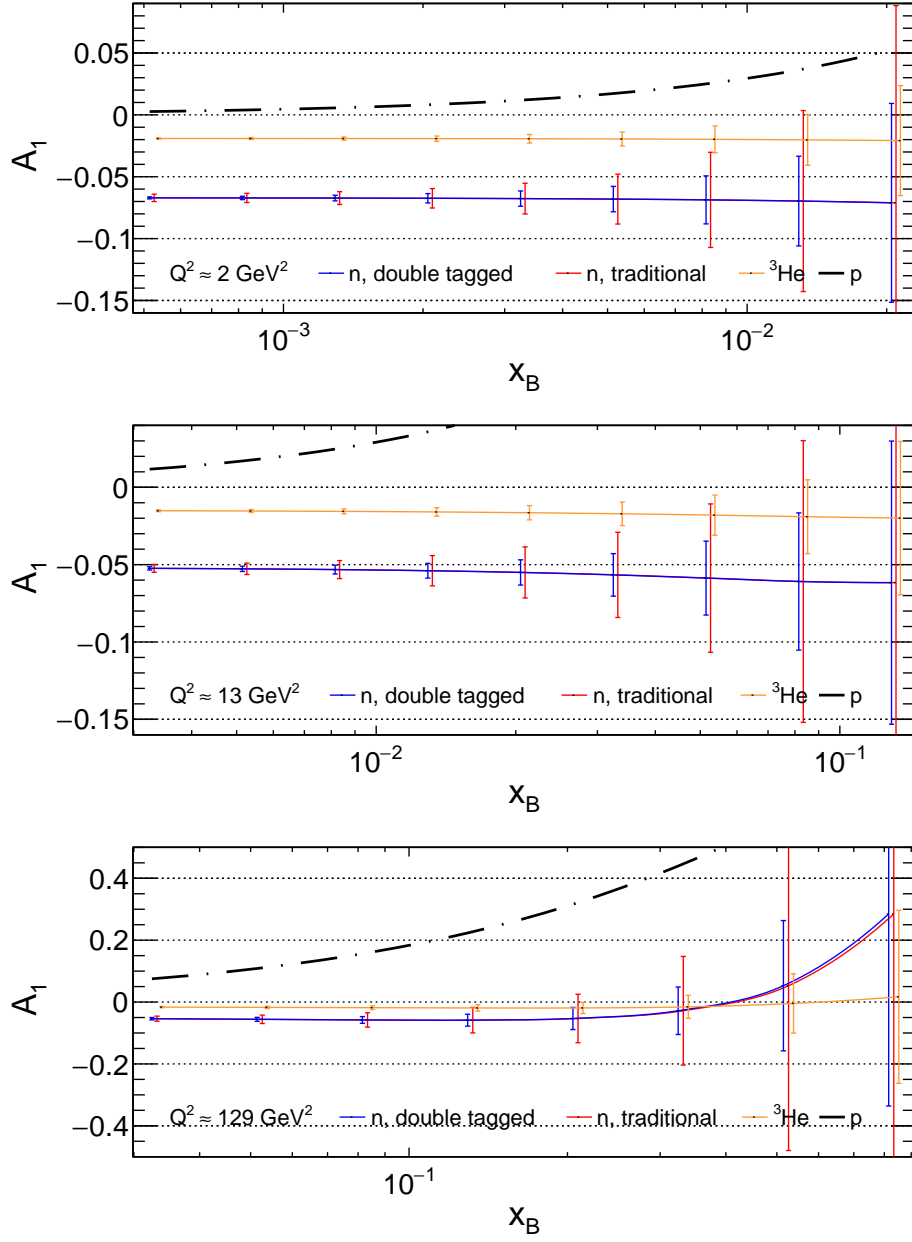


Figure 15: Comparison of  $A_1^n$  uncertainties extracted using the traditional model dependent method (blue) versus the double tagging method (red) at three selected  $Q^2$  bin. The orange line in each plot is the estimated statistical uncertainty of  $A_1^{^3\text{He}}$  while the black dashed line is the central value of  $A_1^p$ .

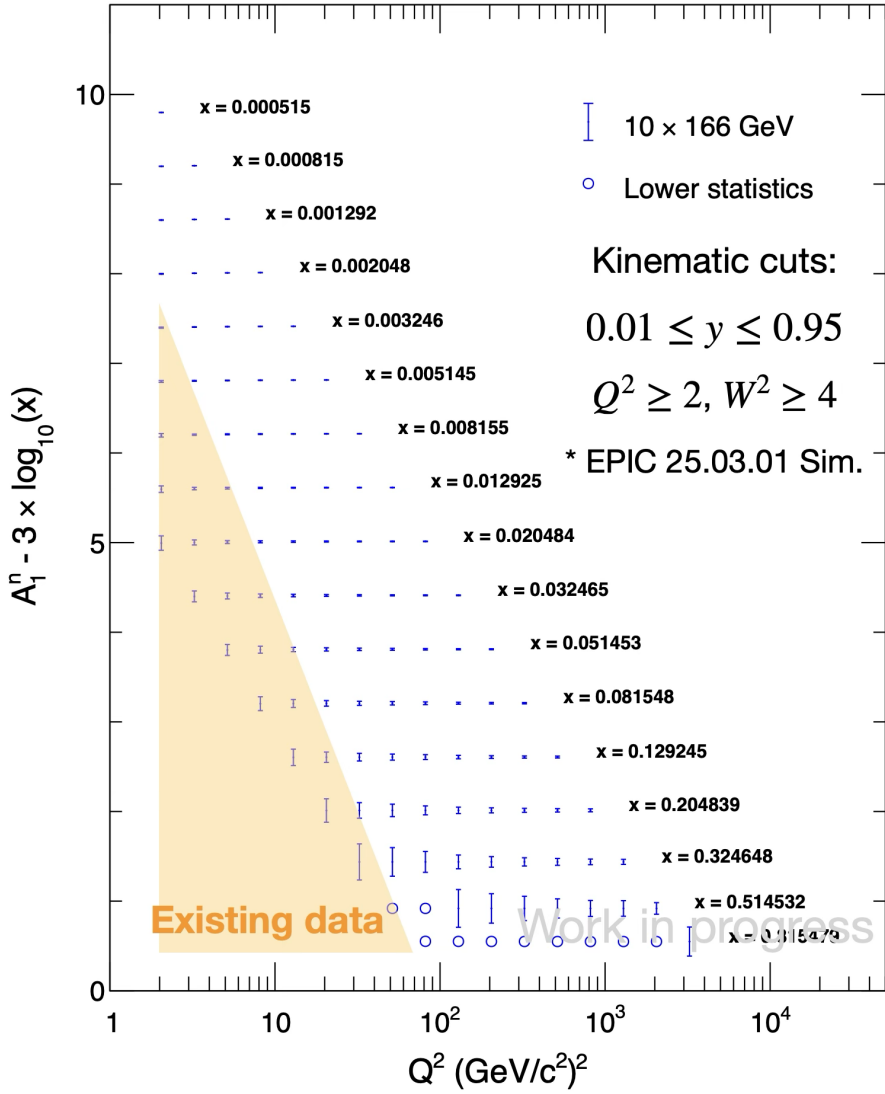


Figure 16: Projected result and statistical uncertainty on  $A_1^n$  in year five of EIC running using the double tagging method described in Sec. 3.2. Central bin  $A_1^n$  value is calculated from parameterization taken from [8]. Highlighted area is the roughly the region of the current existing data on  $A_1^n$ .

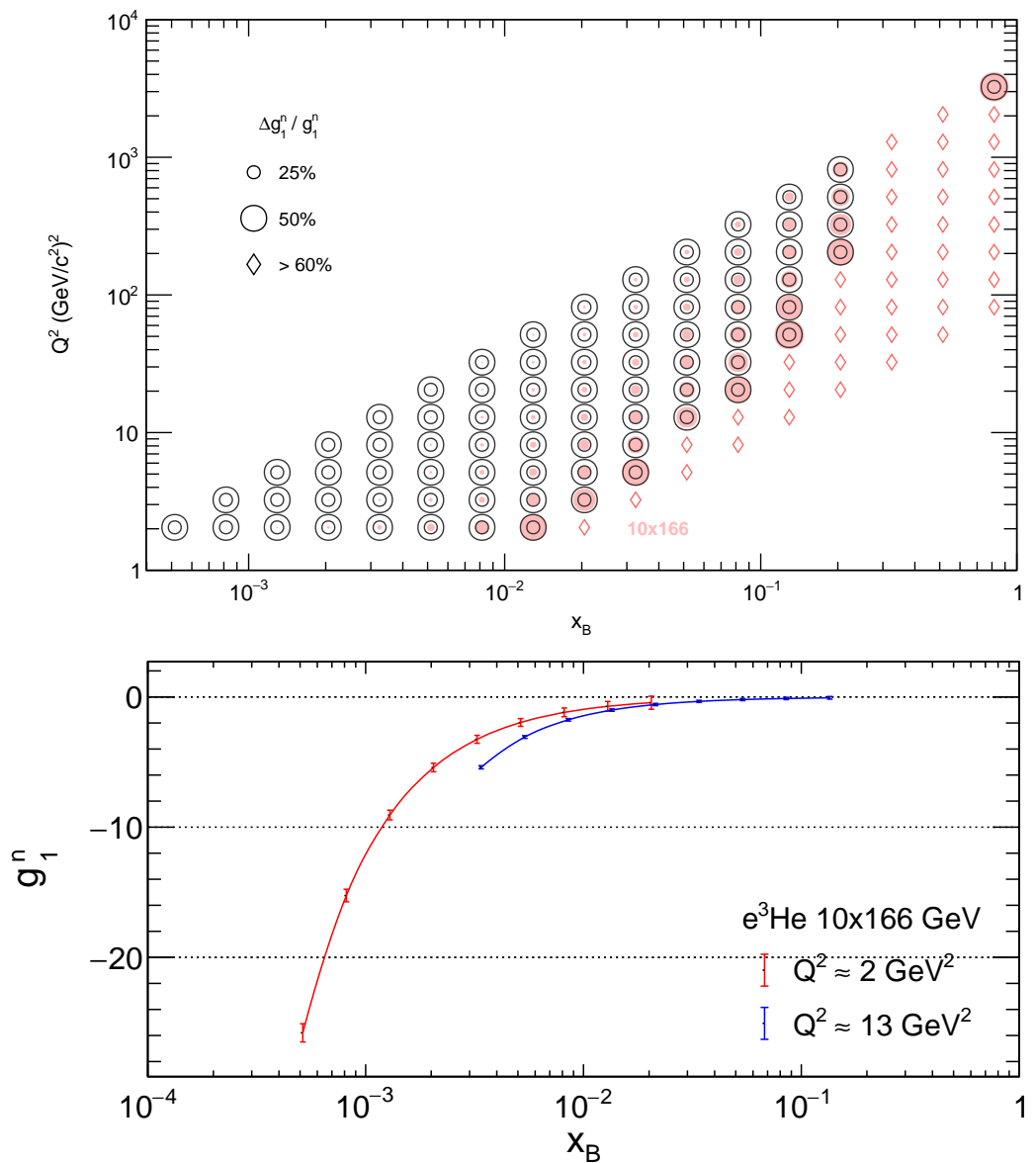


Figure 17: Projected result and statistical uncertainty on  $g_1^n$ .

## 5 Discussion

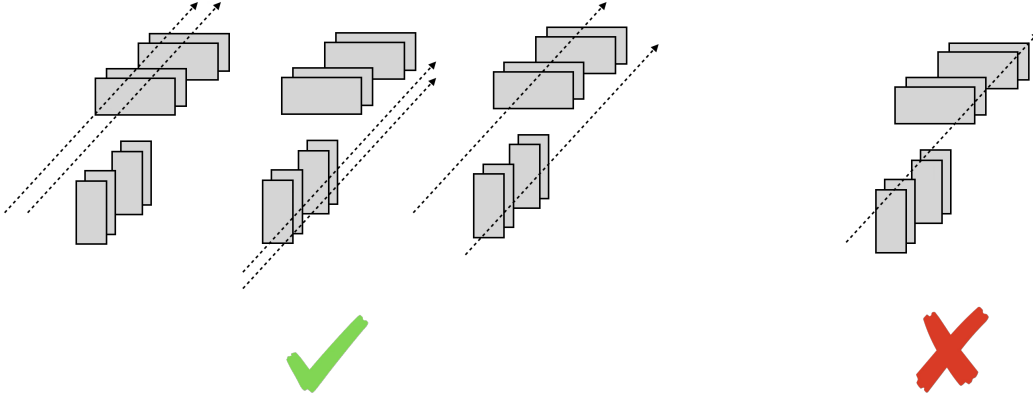


Figure 18: Example spectator tracks in the forward tagging detectors. Left three are examples of tracks that can be successfully tagged by the current simple algorithm. Right is an example event that can cause the algorithm to falsely identify a single spectator as double spectators.

While the current analysis is sufficient to show the kinematic coverage and an estimate of the statistical uncertainty of the  $g_1^n$  measurement in early science time of EIC, more work will be done to improve the result as analysis develop. In this section, examples of future analysis plan is given.

The current tagging algorithm is primitive as indicated earlier in Sec. 3.2. Tracking for the FF detectors is being developed and machine learning model will be used to reconstruct the forward-going proton events. Figure 18 shows example of spectator events that can be successfully tagged using the current algorithm, and an example of the tagging misidentifying from a single tagged event. When the tagging with tracking implemented, the tagging efficiency will be improved, and the statistical uncertainty on  $A_1^{^3\text{He}}$  and  $A_1^n$  will be reduced.

In addtion to a description of the spin structure of neutron,  $g_1^n$  is also valuable for verifying the Bjorken sum and extracting the strong coupling constant,  $\alpha_s$  when combining with the spin structure function of proton,  $g_1^p$ . The Bjorken sum states that:

$$\Gamma_1^{\text{p}-\text{n}} \equiv \int_0^{1^-} (g_1^p - g_1^n) dx \quad (21)$$

where at finite  $Q^2$ , the integral summing the difference between the spin structural function of the proton and neutron across the full Bjorken  $x$  range can be expanded to:

$$\begin{aligned}\Gamma_1^{p-n}(\alpha_s) &= \Gamma_1^{p-n}(Q^2) = \sum_{n>0} \frac{\mu_{2n}^{p-n}(\alpha_s)}{Q^{2n-2}} \\ &= \frac{g_A}{6} \left[ 1 - \frac{\alpha_S(Q^2)}{\pi} - 3.58 \left( \frac{\alpha_S(Q^2)}{\pi} \right)^2 - 20.21 \left( \frac{\alpha_S(Q^2)}{\pi} \right)^3 \right. \\ &\quad \left. - 175.7 \left( \frac{\alpha_S(Q^2)}{\pi} \right)^4 - \mathcal{O}((\alpha_S)^5) \right] \quad (22)\end{aligned}$$

using the  $\bar{MS}$  scheme. In this equation,  $g_A$  is the axial charge,  $\alpha_s$  can be expressed in terms of  $Q^2$ , therefor, by fitting the  $Q^2$  dependence of the Bjorken sum, the double spin assymetry measurment and spin structure functions provide a unique way of determining  $\alpha_s$ .

## 6 Conclusion

ePIC will measure the precise values of  $A_1^{^3\text{He}}$ ,  $A_1^n$  and  $g_1^n$  covering a large kinematic area that is unexplored before. The measurement will provide new data at low x region which is important for studying nucleon spin structure and testing the Bjorken sum rule. With the Far-Forward detectors, ePIC will use a double spectator proton tagging technique to obtain  $A_1^n$  with greater precision than the traditional model dependent extraction method, which is described in details in Sec. 3.2. Starting in year 5 of EIC running, ePIC will have polarized electron and  ${}^3\text{He}$  beam. Roman pots and the Off-Momentum detectors will be installed. ePIC be able to start measuring spin asymmetry and the spin structure function for neutron. The projected result are studied using the latest simulation and analysis, as shown in Sec. 4.

## References

- [1] J. Ellis, R. Jaffe, Sum rule for deep-inelastic electroproduction from polarized protons, Phys. Rev. D 9 (1974) 1444–1446. doi:10.1103/PhysRevD.9.1444.

- [2] J. Ellis, R. Jaffe, Erratum: Sum rule for deep-inelastic electroproduction from polarized protons, Phys. Rev. D 10 (1974) 1669–1670. doi:10.1103/PhysRevD.10.1669.4.
- [3] E. W. Huhhes, R. Voss, Spin structure functions, Annual Review of Nuclear and Particle Science 49 (Volume 49, 1999) (1999) 303–339. doi: <https://doi.org/10.1146/annurev.nucl.49.1.303>.
- [4] X. Zheng, Precision measurement of neutron spin asymmetry  $A_1^N$  at large  $x_{bj}$  using CEBAF at 5.7 GeV, Ph.D. thesis, Massachusetts Institute of Technology (2002).
- [5] W. Chang, et al., Benchmark *ea* generator for lepto production in high-energy lepton-nucleus collisions, Phys. Rev. D 106 (2022) 012007. doi: 10.1103/PhysRevD.106.012007.
- [6] T. Sjöstrand, S. Mrenna, P. Skands, Pythia 6.4 physics and manual, Journal of High Energy Physics 2006 (05) (2006) 026. doi:10.1088/1126-6708/2006/05/026.
- [7] R. Abdul Khalek, et al., Science requirements and detector concepts for the electron-ion collider: EIC yellow report, Nuclear Physics A 1026 (2022) 122447. doi:<https://doi.org/10.1016/j.nuclphysa.2022.122447>.
- [8] X. Zheng, et al., Precision measurement of the neutron spin asymmetries and spin-dependent structure functions in the valence quark region, Phys. Rev. C 70 (2004) 065207. doi:10.1103/PhysRevC.70.065207.
- [9] K. Ackerstaff, et al., Flavor decomposition of the polarized quark distributions in the nucleon from inclusive and semi-inclusive deep-inelastic scattering, Physics Letters B 464 (1) (1999) 123–134. doi:[https://doi.org/10.1016/S0370-2693\(99\)00964-8](https://doi.org/10.1016/S0370-2693(99)00964-8).
- [10] P. L. Anthony, et al., Deep inelastic scattering of polarized electrons by polarized  ${}^3\text{He}$  and the study of the neutron spin structure, Phys. Rev. D 54 (1996) 6620–6650. doi:10.1103/PhysRevD.54.6620.
- [11] K. Ackerstaff, et al., Measurement of the neutron spin structure function  $g_1^n$  with a polarized  ${}^3\text{He}$  internal target, Physics Letters B 404 (3) (1997) 383–389. doi:[https://doi.org/10.1016/S0370-2693\(97\)00611-4](https://doi.org/10.1016/S0370-2693(97)00611-4).

- [12] K. Abe, et al., Measurements of the proton and deuteron spin structure functions  $g_1$  and  $g_2$ , Phys. Rev. D 58 (1998) 112003. doi:10.1103/PhysRevD.58.112003.
- [13] B. Adeva, et al., Spin asymmetries  $A_1$  of the proton and the deuteron in the low  $x$  and low  $Q^2$  region from polarized high energy muon scattering, Phys. Rev. D 60 (1999) 072004. doi:10.1103/PhysRevD.60.072004.
- [14] F. Bissey, A. W. Thomas, I. R. Afnan, Structure functions for the three-nucleon system, Phys. Rev. C 64 (2001) 024004. doi:10.1103/PhysRevC.64.024004.
- [15] C. Cocuzza, W. Melnitchouk, A. Metz, N. Sato, Polarized antimatter in the proton from a global QCD analysis, Phys. Rev. D 106 (2022) L031502. doi:10.1103/PhysRevD.106.L031502.
- [16] A. Buckley, et al., LHAPDF6: parton density access in the LHC precision era, The European Physical Journal C 75 (3) (Mar. 2015). doi:10.1140/epjc/s10052-015-3318-8.
- [17] A. Buckley, et al., The HepMC3 event record library for monte carlo event generators, Computer Physics Communications 260 (2021) 107310. doi:<https://doi.org/10.1016/j.cpc.2020.107310>.
- [18] E. Collaboration, DD4hep Geometry Description of the EPIC Experiment.